R-matrix implementation giving well-behaved quantum defect matrices of molecular hydrogen

Mourad Telmini[1] and Christian Jungen[2]
[1]*Department of Physics, Faculty of Sciences of Tunis, University of Tunis El Manar, 2092 Tunis, Tunisia*
[2]*Laboratoire Aimé Cotton du CNRS, Université de Paris-Sud, 91405 Orsay, France*
(Received 23 May 2003; published 17 December 2003)

The *ab initio* variational *R*-matrix method is combined with generalized quantum-defect theory to calculate quantum defect matrices for $^1\Sigma_u^+$ and $^1\Pi_u$ symmetries of molecular hydrogen. The calculations take account of doubly excited channels and are optimized so as to minimize the dependence of the quantum-defect matrix elements as functions of energy and internuclear distance. The matrices are used to calculate the lowest clamped-nuclei Rydberg potential energy curves as well as doubly excited resonance positions and widths near the first excited state of H_2^+. The results are in good agreement with previous *ab initio* results. Owing to their smoothness, the quantum-defect matrices are well suited for rovibronic multichannel quantum-defect applications. This opens up the possibility of a fully *ab initio* quantitative theoretical description of excited H_2, including ionization and dissociation.

DOI: 10.1103/PhysRevA.68.062704 PACS number(s): 34.60.+z, 31.10.+z, 31.25.−v, 34.80.Kw

I. INTRODUCTION

Multichannel quantum defect theory (MQDT) [1,2] no doubt is the most successful method able to describe the complicated rovibronic multichannel phenomena arising in molecules near ionization or photodetachment thresholds. Rovibronic channel interactions mediate the conversion of electronic energy into energy of nuclear motion (or vice versa), and hence are the source of nonadiabatic chemical dynamics in excited molecules. Manifestations of such dynamics range from anion formation in molecular clusters by slow electron collisions [3], to dissociative recombination processes important for interstellar chemistry [4].

One of the attractive features of multichannel quantum-defect theory is the way it accounts for resonant phenomena, by adding closed fragmentation channels explicitly to the system of open scattering (continuum) channels arising in the standard formulation of scattering theory. The relevant scattering information is then represented by additional rows and columns of the thus ''extended'' scattering (or equivalent quantum-defect) matrices. These vary smoothly with energy as the resonances have been eliminated, and they do not exhibit the often near-random resonant behavior due to the details of the spectroscopy of the molecule under study. Another central element of molecular MQDT is that by means of suitable transformations of the frame of reference of the colliding partners (so-called frame transformations), MQDT relates the rovibronic collision matrices to corresponding fixed-nuclei quantities—typically energy- and nuclear-geometry-dependent quantum-defect matrices $\mu(E,R)$—from which the nuclear dynamics has been removed, but which nevertheless contain the relevant scattering information necessary to account for nonadiabatic transfer of energy between the electrons and nuclei.

From the point of view of theory, it appears desirable to be able to calculate the extended body frame quantum defects directly in an *ab initio* procedure, just as the potential-energy curves or surfaces of a molecule are obtained by use of standard quantum-chemical codes. In order to be useful in practice in the framework of quantum defect theory, these *ab initio* quantum-defects should vary rather smoothly with energy and molecular geometry. The double smoothness is necessary because (i) the inclusion of the vibrational degree(s) of freedom requires the evaluation of vibrational integrals with the phase shift or quantum-defect functions as kernels, and (ii) the validity of the frame-transformation method requires (see, e.g., Ref. [5]) that the phase shifts or quantum defects depend only mildly on the energy. If we disregard nuclear motion entirely (by bypassing the frame-transformation procedure), we can still use MQDT (i.e., solve the extended collision problem) for fixed geometry and negative energies, to obtain the clamped-nuclei bound Rydberg potential-energy curves. A further quality requirement for the quantum-defect matrices then is that these potential curves should be of reasonable accuracy, giving a realistic account of the lowest molecular states over an adequate range of geometries.

While a vast amount of *ab initio* work has been devoted to molecular photoionization processes and low-energy electron collisions in general, only few papers have been published where the body frame quantum defects were calculated directly in the continuum as well as in the bound-state energy range. As far as neutral molecular (Rydberg) systems are concerned, the pioneering calculations are those of Stephens and McKoy [6] who used Schwinger's variational principle to obtain quantum defects for H_2 for the bound-state range. Their work was restricted to the independent electron approximation however, and took account only of the ground-state ion core. A few years later Greene and Yoo [7] presented calculations also for H_2, which took account of electron correlation and included core-excited channels explicitly. These authors treated bound and continuum states using the variational eigenchannel *R*-matrix method [8,9] which is based on Kohn's original ideas [10]. Their work was similar in spirit to that of Ross and Jungen [11] except that these latter authors derived the quantum-defect matrices from existing quantum-chemical potential-energy curves rather than carrying out their own *ab initio* calculations.

The use of the variational *R*-matrix theory for molecular problems has been initiated by Raseev and Le Rouzo

[12,9,13]. The Wigner-Eisenbud *R*-matrix formulation has been used by Tennyson, Noble, and Salvini [14], Tennyson and Noble [15], and Shimamura, Noble, and Burke [16] to calculate continuum resonances in H_2. Other applications of the Wigner-Eisenbud formalism include Rydberg and valence excitations in molecules such as CH [17], HeH [18], and NO [19]. An important paper to be mentioned here is that by Hiyama and Child [20] who combined the Wigner-Eisenbud formalism with multichannel quantum-defect theory to calculate diabatic Rydberg and valence-state potential energy curves of NO. The Schwinger variational principle has been used by Lucchese and co-workers [21] in an approach that also accounts for electron correlation, both in the description of the interchannel interactions and in the representation of the target ions. The applications of this method to the photoionization of CO, N_2, and NO have been very successful. However, only open channels appear explicitly in the coupled-channels treatment carried out in this approach. While electronic interchannel coupling is taken into account, it leads to the occurrence of electronic autoionization resonances, i.e., strongly energy-dependent continuum phase shifts, which are undesirable from the present point of view.

Despite the fact that the *R*-matrix method today is basically a well-established theoretical tool for calculating highly excited bound as well as continuum states of atoms and molecules, applications to molecules have often been plagued by practical problems of various sorts, and therefore have unfortunately remained limited to few systems and few symmetries. The central purpose of our present work is to eliminate two major drawbacks of some of the earlier work, namely, the unsatisfactory accuracy of the purely *ab initio* results and/or the excessive variations with internuclear distance and energy of the quantum-defect matrices obtained in the calculations. For example, the calculations of Stephens and McKoy [6] yielded quite smooth quantum defect functions. However, since these calculations were restricted to the independent electron approximation they produced clamped-nuclei potential-energy curves of reasonable accuracy only near equilibrium (with an error of about 3000 cm^{-1}), while becoming entirely unrealistic at larger internuclear distances. Greene and Yoo [7] on the other hand were able to obtain clamped-nuclei quantum defects correct to better than about 0.05 over a considerable range of geometries. This accuracy corresponds to an error of the clamped-nuclei electronic potential-energy curves of less than 1500 cm^{-1} for $n=2$ or 50 cm^{-1} for $n=6$. Their quantum-defect matrices, however, exhibit such strong variations with energy and internuclear distance that they cannot be used in the framework of rovibronic quantum-defect theory.

Our present approach is in many ways similar to the work of Greene and Yoo [7]. We combine the elliptical effective one-electron treatment applied to dipolar diatomic molecules by Arif *et al.* [22], with the effective two-electron approach developed for atomic applications by Aymar and *et al.* [23], and we also make use of the phase-amplitude description of strongly closed core-excited electron channels implemented in Ref. [24]. Specifically we shall show how careful consideration of the elliptical *R*-matrix boundary ξ_0, together with an optimized choice of the regular and irregular (sin and cos type) radial reference scattering functions for the core-excited closed channels, allows the energy and nuclear-coordinate dependences of the quantum-defect matrices to be largely removed.

In a later step we plan to combine the *ab initio* quantum-defect matrices with rovibronic quantum-defect theory and frame-transformation theory, so as to be able to make accurate *ab initio* predictions for the spectra and dynamics (electronic, vibrational, and rotational autoionization competing with predissociation, multiphoton excitations) on the scale of rotational energy resolution. In the present paper we limit ourselves to the dipole-allowed $^1\Sigma_u^+$ and $^1\Pi_u$ channels of H_2. Unless specified otherwise, energies will be expressed throughout the paper in rydbergs, and lengths in bohrs.

II. THEORY

The nuclei are assumed located at the fixed points *A* and *B* separated by the internuclear distance *R*, and prolate spheroidal coordinates (ξ,η,φ) are used for the electrons,

$$\xi=\frac{r_A+r_B}{R} \quad (\xi\in[1,+\infty]) \tag{1}$$

$$\eta=\frac{r_A-r_B}{R} \quad (\eta\in[-1,+1])$$

with $\varphi\in[0,2\pi]$ being the azimuthal angle. r_A and r_B are the distances of an electron from each nucleus.

The electron configuration space is divided into an inner reaction zone and an outer asymptotic zone. The reaction volume is defined by $\max(\xi_1,\xi_2)\leqslant\xi_0$, and ξ_0 will be chosen large enough so that one may assume that only one electron at a time is allowed to leave this internal region. Strictly speaking, the reaction volume is a five-dimensional hypersurface which may be visualized as an ellipsoid with the two nuclei placed at its focal points. Inside the reaction zone all of the interactions between the two electrons will be taken into account, i.e., the full multipolar expansion of the electron-electron Coulomb interaction $2/r_{12}$ and exchange interactions. The asymptotic or external region includes all of the remaining space. ξ_0 must be large enough so that the escaping electron comes across just a two-center Coulomb field plus a medium-range polarization field, with the screening charge of the internal electron being shared equally between the two nuclei.

A. One-electron functions in the internal zone

We start by defining one-electron basis functions for $\xi\leqslant\xi_0$. Each spheroidal orbital corresponding to a given value λ of the orbital angular momentum projection onto the internuclear axis is written as a product:

$$\phi(\xi,\eta,\varphi)=\frac{\tilde{X}(\xi)}{\sqrt{\xi^2-1}}\tilde{Y}(\eta,\varphi)\equiv\frac{\chi(\xi)}{\sqrt{\xi^2-1}}\frac{\zeta(\eta)}{\sqrt{1-\eta^2}}\frac{1}{\sqrt{2\pi}}e^{i\lambda\varphi}. \tag{2}$$

Each function is a solution of the Schrödinger equation for the two-center problem which has been discussed many times in the literature. The identity on the right-hand side of Eq. (2) serves to precisely relate the radial functions $\chi(\xi)$ and angular functions $\zeta(\eta)$ used in the present work, to the equivalent radial functions $\tilde{X}(\xi)$ and elliptical harmonics $\tilde{Y}(\eta,\varphi)$ defined and discussed in detail in Appendix B of Ref. [22]. Note that the elliptical harmonics depend on the energy, but that for given energy they form an orthonormal subset of functions with volume element $d\eta d\varphi$.

As in Ref. [22], both $\chi(\xi)$ and $\zeta(\eta)$ are obtained by direct numerical integration of the appropriate differential equations [Eqs. (B7) and (B8) of Ref. [22] with $Z_1=Z_1^{eff}=Z_2=Z_2^{eff}=1,\alpha_1=\alpha_2=0$]. We impose a regular behavior on ζ for $\eta=\pm 1$ and on χ for $\xi=1$ [$\zeta(\pm 1)=0,\chi(1)=0$], whereas, as will be specified later, for $\xi=\xi_0$ we impose a fixed boundary condition on each χ, $b=-\chi'/\chi$ (where the $'$ indicates the derivative with respect to the radial coordinate ξ). This procedure yields a discrete set of functions with eigenenergies E_i, where $i\equiv(n\tilde{l}\lambda)$, $n-\tilde{l}-1$ is the number of nodes of the radial function, and $\tilde{l}-\lambda$ is the number of nodes of the angular function ζ as in Ref. [22]. Note that $\tilde{l}$ reduces to the familiar spherical angular momentum quantum number l when $R\to 0$ [22].

One-electron overlap matrix elements will be required below and are calculated with the volume element $(R/2)^3(\xi^2-\eta^2)d\xi d\eta d\varphi$ as

$$o_{ii'}=\left(\frac{R}{2}\right)^3\delta_{\lambda_i\lambda_{i'}}\left\{\int_1^{\xi_0}\chi_i(\xi)\chi_{i'}(\xi)d\xi\int_{-1}^{+1}\frac{\zeta_i(\eta)\zeta_{i'}(\eta)}{1-\eta^2}d\eta+\int_1^{\xi_0}\frac{\chi_i(\xi)\chi_{i'}(\xi)}{\xi^2-1}d\xi\int_{-1}^{+1}\zeta_i(\eta)\zeta_{i'}(\eta)d\eta\right\}. \quad (3)$$

B. Two-electron basis functions in the internal zone

Normalized two-electron basis functions are constructed as Slater-type products of one-electron functions as follows:

$$y_{ij}(\xi_1,\eta_1,\varphi_1,\xi_2,\eta_2,\varphi_2)=\frac{1}{\sqrt{2N_{ij}}}\{\phi_i(\xi_1,\eta_1,\varphi_1)\phi_j(\xi_2,\eta_2,\varphi_2)+(-1)^S\phi_j(\xi_1,\eta_1,\varphi_1)\phi_i(\xi_2,\eta_2,\varphi_2)\}, \quad (4)$$

where

$$N_{ij}=o_{ii}o_{jj}+(-1)^S o_{ij}o_{ji}. \quad (5)$$

Each basis function y_{ij} is thus specified by the six quantum numbers as $n_1\tilde{l}_1\lambda_1 n_2\tilde{l}_2\lambda_2$, where in the following, antisymmetrization with respect to the exchange operation according to Eq. (4) will be implied. *Gerade (g)* and *ungerade (u)* functions are obtained by selecting $\tilde{l}$ values such that $\tilde{l}_1+\tilde{l}_2$ is *even* or *odd*, respectively. λ_1 and λ_2 are selected such as to correspond to the desired value $\Lambda=\lambda_1+\lambda_2$. Note that we are using signed quantum numbers Λ here, so that the basis functions y_{ij} do not necessarily transform as $+$ or $-$ under the symmetry operation σ_v corresponding to a reflection at a plane containing the nuclei. This means that Σ^+ and Σ^- channels are not distinguished in our calculations, but in practice this is of no consequence since Σ^- channels become relevant in H_2 at energies far higher than the range considered here. Two-electron overlap matrix elements will also be required later and take the form

$$O_{ij,i'j'}=\frac{1}{\sqrt{N_{ij}N_{i'j'}}}[o_{ii'}o_{jj'}+(-1)^S o_{ij'}o_{i'j}]. \quad (6)$$

Equation (6) shows that the basis functions y_{ik} are normalized to unity.

C. Bielectronic integrals

The evaluation of the bielectronic integrals is a delicate matter and represents a crucial step in the calculation. Following earlier work [25,26,7,27], we expand the electron-electron distance $1/r_{12}$ in terms of associated Legendre functions as

$$\frac{1}{r_{12}}=\frac{2}{R}\sum_{l=0}^{\infty}\sum_{\mu=-l}^{l}(-1)^{|\mu|}(2l+1)\times\left(\frac{(l-|\mu|)!}{(l+|\mu|)!}\right)^2 Q_l^{|\mu|}(\xi_>)P_l^{|\mu|}(\xi_<)\times P_l^{|\mu|}(\eta_1)P_l^{|\mu|}(\eta_2)e^{i\mu(\varphi_1-\varphi_2)}, \quad (7)$$

where $\xi_>$ and $\xi_<$ are the larger and the smaller of ξ_1 and ξ_2 as usual. The functions $P_l^{|\mu|}(\xi)$ and $Q_l^{|\mu|}(\xi)$ are the associated Legendre functions of the first kind and the second kind, respectively. Their numerical evaluation is described in the Appendix.

The interaction matrix elements $[1/r_{12}]_{ij,i'j'}$ are calculated by numerical integration. Note that as the symbolic coordinates $\xi_>$ and $\xi_<$ are replaced by ξ_1 and ξ_2, respectively, the divergence at the origin of the functions $Q_l^{|\mu|}(\xi)$ in Eq. (7) turns out to be compensated by the regular behavior of the functions $P_l^{|\mu|}(\xi)$ and of the single-electron radial basis functions $\chi(\xi)$.

D. Variational *R*-matrix calculation

Once a suitable basis set has been chosen, a Hamiltonian matrix can be set up in the reaction volume:

$$H_{ij,i'j'}=(E_{i'}+E_{j'})O_{ij,i'j'}+2\left[\frac{1}{r_{12}}\right]_{ij,i'j'}. \quad (8)$$

Diagonalization of this matrix yields eigenvalues and eigenfunctions of the two-electron Hamiltonian in the reaction volume. These eigenenergies and eigenfunctions depend on ξ_0 and also on the value $-b(\xi_0)$ imposed on the logarithmic derivative of each basis function at ξ_0. $b(\xi_0)$ may be taken to be the same for all basis functions and its value may be

varied iteratively. The eigenvalues of the Hamiltonian matrix will then vary correspondingly. If an eigenvalue of H can be made to coincide with the preselected total energy E, $b(\xi_0)$ can be considered to be an eigenvalue b_β of the boundary condition compatible with that energy. This is the iterative eigenchannel procedure of Fano and Lee [28].

In the variational R-matrix scheme such as formulated by Greene [8], one uses simultaneously a whole ''basis'' of different boundary conditions $b(\xi_0)$, to be specified later' and one solves a generalized eigenvalue system of the form

$$\Gamma\vec{c}=b(E,\xi_0)\Lambda\vec{c}, \tag{9}$$

which directly yields the set of eigenvalues $b_\beta=-\Psi'_\beta/\Psi_\beta$, for the boundary condition on the reaction surface ξ_0 compatible with E. The associated set of coefficients c_{ij}^β serves to construct the eigenfunctions valid in the reaction volume in terms of the basis functions of Eq. (4):

$$\Psi_\beta=\sum_{ij} c_{ij}^\beta y_{ij}. \tag{10}$$

For a given preselected total energy E the matrix elements of Γ and Λ of Eq. (9) are defined as follows:

$$\Gamma_{ij,i'j'}=2(EO_{ij,i'j'}-H_{ij,i'j'}-L_{ij,i'j'}) \tag{11}$$

and

$$\Lambda_{ij,i'j'}=\frac{R}{2}\delta_{\lambda_j\lambda_{j'}}o_{ii'}\chi_j(\xi_0)\chi_{j'}(\xi_0)\int_{-1}^{+1}\frac{\zeta_j(\eta)\zeta_{j'}(\eta)}{1-\eta^2}d\eta, \tag{12}$$

with $H_{ij,i'j'}$ as given in Eq. (8), and with the elements of the Bloch matrix L given by

$$L_{ij,i'j'}=\frac{R}{2}\chi_j(\xi_0)\left\{\delta_{\lambda_j\lambda_{j'}}o_{ii'}\chi'_{j'}(\xi_0)\int_{-1}^{+1}\frac{\zeta_j(\eta)\zeta_{j'}(\eta)}{1-\eta^2}d\eta + (-1)^S\delta_{\lambda_j\lambda_{i'}}o_{ij'}\chi'_{i'}(\xi_0)\int_{-1}^{+1}\frac{\zeta_j(\eta)\zeta_{i'}(\eta)}{1-\eta^2}d\eta\right\}. \tag{13}$$

The primes on the radial functions χ in Eq. (13) refer here again to the derivative with respect to the radial coordinate ξ. The surface element used for the integrations in Eqs. (12) and (13) is [29] $d\sigma=dv_<d\sigma_>$ with $d\sigma_>=(R/2)^2\sqrt{\xi_0^2-1}\sqrt{\xi_0^2-\eta^2}d\eta d\varphi$ and $dv_<$ as indicated before Eq. (3). Note that the angular integral in Eqs. (12) and (13) does not reduce to $\delta_{jj'}$ in the present elliptical formulation because the $\zeta(\eta)$ functions are orthogonal only if corresponding to the same energy.

E. One-electron channel wave functions in the external zone

For ξ values larger than ξ_0, the two-electron problem reduces to a one-electron problem which is separable in prolate spheroidal (elliptical) coordinates. Each channel can be labeled in the external zone as $k\equiv(n_1\tilde{l}_1\lambda_1)\epsilon\tilde{l}_2\lambda_2$. The radial and angular functions of the single electron present in the external zone are evaluated numerically in an analogous manner as the one-electron basis functions discussed in Sec. II A with the following differences.

(i) We set $Z_1=Z_1^{eff}=Z_2=Z_2^{eff}=\frac{1}{2},\alpha_1=\alpha_2=\frac{1}{2}\alpha(R)$ in Eqs. (B7) and (B8) of Ref. [22] in order to account for the partial screening of the protons by the core electron and to include the dipole polarization field of the core. $\alpha(R)$ is the spherical component of the dipole polarization tensor of H_2^+ (see Ref. [22]) which we take to be the same in the $1\tilde{s}\sigma$ and $2\tilde{p}\sigma$ core states.

(ii) The numerical propagation of the radial function must be carried to an appropriately large ξ value (in principle infinity).

(iii) We evaluate radial channel functions for channel energies $\epsilon_c=E-E_c$, where E is the arbitrarily preselected total energy. For each energy and each core state we evaluate solutions that are regular at the origin, $f_k(\epsilon_c,\xi)$, as well as solutions that are irregular, $g_k(\epsilon_c,\xi)$.

Specifically, we calculate the radial channel functions in phase-amplitude form

$$f_k(\epsilon_c,\xi)=\sqrt{\frac{1}{\pi}}\alpha_k(\epsilon_c,\xi)\sin\int_1^\xi\frac{1}{\alpha_k^2(\epsilon_c,\xi')}d\xi' \tag{14}$$

and an analogous expression for $g_k(\epsilon_c,\xi)$ with sin replaced by $-\cos$. The normalization in Eq. (14) corresponds to a value of the Wronskian $W(f_k,g_k)=1/\pi$ (see Ref. [24]). Note that f, g, and α depend on the channel electron energy ϵ_c as well as on $\tilde{l}$ and λ. $\alpha_k(\epsilon_c,\xi)$ is the amplitude function which is smooth, i.e., does not have the nodes characterizing f and g, and it obeys Milne's inhomogeneous differential equation [30]. Recipes for its numerical integration for arbitrary energy are discussed, e.g., in Ref. [24]. The amplitude function $\alpha_k(\epsilon_c,\xi)$ is asymptotically divergent for negative channel energies ϵ_c, i.e., below the ionization threshold E_c, and the same is therefore generally true for the channel functions f and g. However, we see from Eq. (14) that the *accumulated phase* $\beta_k(\epsilon_c)=\int_1^\infty\alpha_k^{-2}(\epsilon_c,\xi)d\xi$ is finite, so that asymptotically we have

$$f_k(\epsilon_c,\xi)\sim\sqrt{\frac{1}{\pi}}\alpha_k(\epsilon_c,\xi)\sin\beta_k(\epsilon_c) \tag{15}$$

and an analogous expression for $g_k(\epsilon_c,\xi)$. The numerical evaluation of the amplitude function $\alpha_k(\epsilon_c,\xi)$ and the associated accumulated phase $\beta_k(\epsilon_c)$ becomes a somewhat delicate matter at very low energies when a channel becomes ''strongly closed,'' i.e., below the lowest eigenvalue associated with the radial potential where $\beta_k(\epsilon_c)/\pi\leqslant 1$. This situation has been considered in detail in Ref. [24] and is indeed encountered in H_2: as $R\to 0$, the energy of the $2\tilde{p}\sigma$ repulsive core is rising, and the core-excited channels associated with it therefore become increasingly strongly closed in the energy region where the Rydberg spectrum associated with the ground state core occurs.

F. Matching procedure on the surface of the reaction volume

Each variational solution Ψ_β of Eq. (10) may be continued in the asymptotic zone, i.e. for radii larger than ξ_0, as a linear combination of the regular and irregular radial channel functions and as a sum over channel components *i*:

$$\Psi_\beta(E,\omega,\xi)=\sum_k \Phi_k(E,\omega)\frac{1}{\sqrt{\xi^2-1}} \times[f_k(\epsilon_c,\xi)I_{k\beta}-g_k(\epsilon_c,\xi)J_{k\beta}], \quad (16)$$

where ω denotes all coordinates except ξ, $\omega \equiv(\xi_1,\eta_1,\varphi_1,\eta_2,\varphi_2)$. The sum over k extends over the ''physically relevant'' channels, i.e., those that are weakly closed in the usual sense of quantum-defect theory. The matrices I and J consist of matching coefficients which we shall now determine by requiring that Eq. (16) and its derivative with respect to ξ be continuous at $\xi=\xi_0$, i.e., the outer-zone solution Eq. (16) must join on smoothly to the inner-zone variational solution Eq. (10). The short-range reaction matrix K is then obtained as

$$K_{kk'}=\sum_\beta J_{k\beta}I^{-1}_{k'\beta}. \quad (17)$$

In an initial step we expand the inner-zone variational solution Ψ_β on the reaction surface in terms of the so-called ''surface harmonics''

$$\Phi_k(E,\omega)=\phi_c(\xi_1,\eta_1,\varphi_1)\frac{\zeta^{\epsilon_c}_{\tilde{l}_2\lambda_2}(\eta_2)}{\sqrt{1-\eta^2}}\frac{e^{i\lambda_2\varphi_2}}{\sqrt{2\pi}}. \quad (18)$$

For each given total energy E and channel k, the full set of surface harmonics $\Phi_k(E)$ is orthogonal and complete on the surface Σ, although in practice the expansion will be restricted to the physically relevant channels. This is sufficient because if ξ_0 is chosen large enough, the expansion Eq. (10) will no longer contain the physically ''irrelevant'' channels present at shorter range.

The expansion coefficients are obtained by projection,

$$u_{k\beta}(E,\xi_0)=\int_\Sigma \Phi_k(E,\omega)\Psi_\beta(E,\omega,\xi_0)d\omega, \quad (19)$$

and we also have

$$u'_{k\beta}(E,\xi_0)=-b_\beta(E)u_{k\beta}(E,\xi_0), \quad (20)$$

where the prime again indicates to differentiation with respect to ξ.

Subtraction of Eq. (20) from Eq. (19) after multiplication by g'_k and g_k, or f'_k and f_k, respectively, leads to

$$I_{k\beta}=\pi W(u_{k\beta},g_k),$$
$$J_{k\beta}=\pi W(u_{k\beta},f_k), \quad (21)$$

where we have used the fact that the Wronskian $W(f_k,g_k)$ is equal to $1/\pi$.

It remains to spell out the integral of Eq. (19) explicitly, by expressing $\Psi_\beta(E,\xi_0)$ in terms of the two-electron basis functions y_{ij} of Eq. (4) with the coefficients c^β_{ij} defined by Eq. (9). We find

$$u_{k\beta}(E,\xi_0)=\sum_{ij} c^\beta_{ij}\chi^o_j(\xi_0)\delta_{ci}\delta_{\lambda_j\lambda_k}\int_{-1}^{+1}\frac{\zeta^{\epsilon_c}_k(\eta)\zeta_j(\eta)}{1-\eta^2}d\eta. \quad (22)$$

The angular integral in Eq. (22) does not reduce exactly to δ_{jk} unless the $\zeta(\eta)$ functions are calculated at the same energy, i.e., $E_j=E\equiv\epsilon_c+E_c$.

III. DETAILS OF CALCULATIONS

A. Asymptotic channels and *R*-matrix radius

Our present application concerns an energy range extending from the lowest $^1\Sigma^+_u$ bound state of H_2 up to the $2\tilde{p}\sigma$ excited ionization threshold. Therefore we explicitly include in the external zone all channels built on the $1\tilde{s}\sigma$ and $2\tilde{p}\sigma$ ions with $\tilde{l}\leqslant 3$, namely, the $1\tilde{s}\sigma\epsilon\tilde{p}\sigma$, $1\tilde{s}\sigma\epsilon\tilde{f}\sigma$, $2\tilde{p}\sigma\epsilon\tilde{s}\sigma$, and $2\tilde{p}\sigma\epsilon\tilde{d}\sigma$ channels for $^1\Sigma^+_u$ symmetry, and the $1\tilde{s}\sigma\epsilon\tilde{p}\pi$, $1\tilde{s}\sigma\epsilon\tilde{f}\pi$, and $2\tilde{p}\sigma\epsilon\tilde{d}\pi$ channels for $^1\Pi_u$ symmetry.

The choice of the *R*-matrix radius ξ_0 is subject to two conflicting requirements. First of all, we must choose ξ_0 large enough so that the two lowest states of H_2^+ that arise explicitly in the channel treatment are enclosed within it. At the same time we wish to take the *R*-matrix radius as small as possible in order to avoid a situation where the innermost lobe of the Rydberg electron function is fully included within it, giving rise to a resonant behavior of the quantum defect at low energy. To say it pointedly, we wish, e.g., the $2\tilde{p}\sigma$ core of the configuration $2\tilde{p}\sigma 1\tilde{s}\sigma$ to be contained within ξ_0, and at the same time the $2\tilde{p}\sigma$ Rydberg orbital of the configuration $1\tilde{s}\sigma 2\tilde{p}\sigma$ to extend beyond ξ_0. In practice a compromise could be found for each R value after some experimenting, by requiring that (i) the eigenenergies of the lowest two one-electron functions within the reaction volume should differ from the exact eigenvalues of H_2^+ by no more than about 10^{-3} Ry, and (ii) the bound states calculated for H_2 (see Sec. IV) should not vary significantly when ξ_0 is varied. The ξ_0 values adopted finally are the smallest satisfying both requirements, and correspond approximately to $\xi_0\approx -2.5+3.5\xi_{cl}(R)$ where $\xi_{cl}(R)$ is the classical reflection point for the core electron in the $2\tilde{p}\sigma$ orbital at internuclear distance R. The values of the spherical polarizability $\alpha(R)$ of H_2^+ have been taken from Bishop and Cheung [31] and were used according to the prescription given in Ref. [22].

B. One-electron and two-electron functions

The variational *R*-matrix approach requires basis functions corresponding to at least two distinct boundary conditions on the boundary of the reaction volume. Following earlier applications of the variational *R*-matrix scheme, we use a

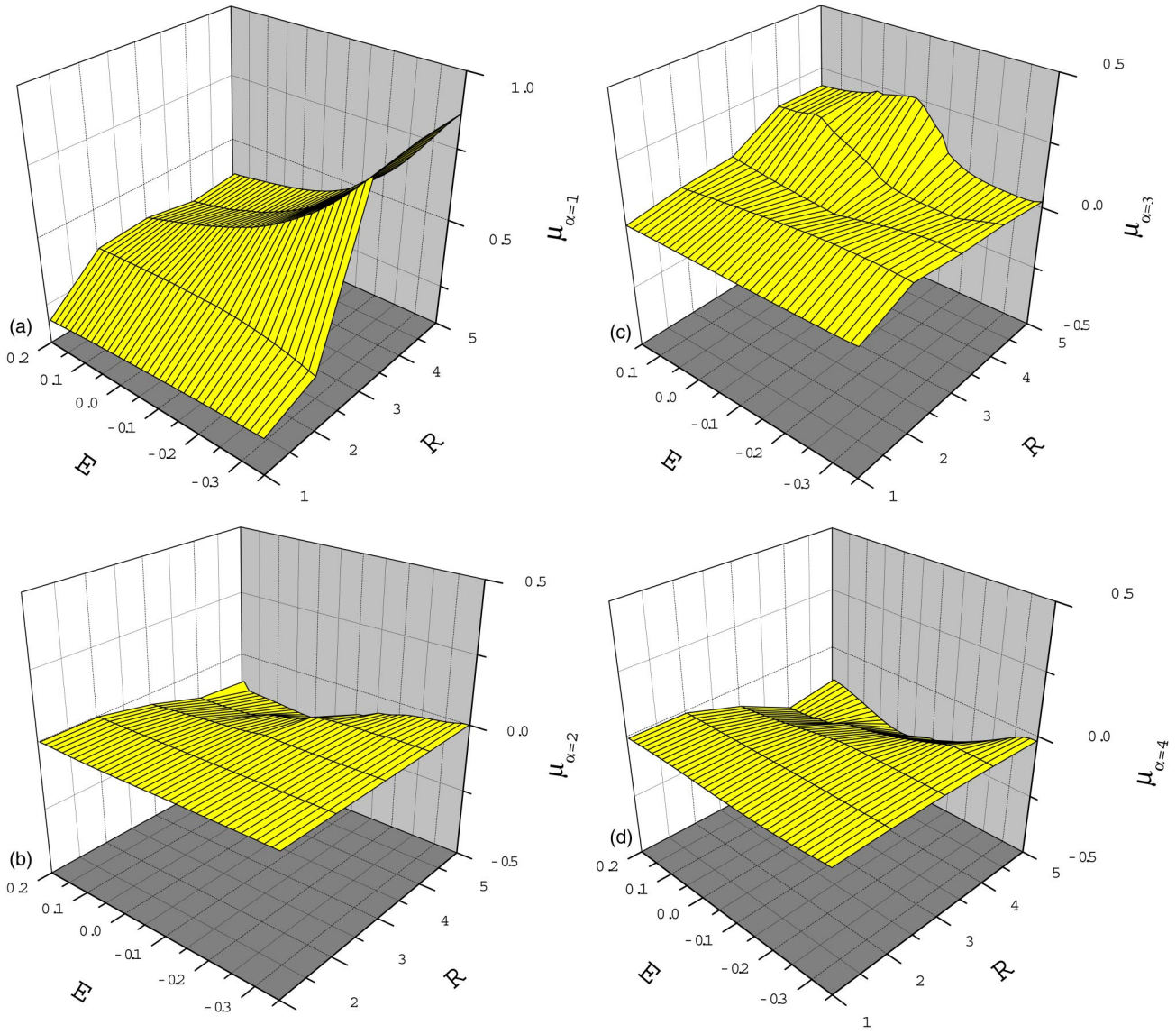

FIG. 1. *Ab initio* eigenquantum defects for $^1\Sigma_u^+$ symmetry as functions of internuclear distance R in atomic units and energy E in rydbergs. The zero of energy corresponds to the H_2^+ $1s\sigma$ threshold. (a) $\alpha=1$, (b) $\alpha=2$, (c) $\alpha=3$, (d) $\alpha=4$. Note the different origin of the quantum defect scale employed for $\alpha=1$. See text for details.

large set of ''closed'' functions corresponding to $\chi^c(\xi=\xi_0)=0$, as well as a small additional set of ''open'' functions $\chi^o(\xi)$ with $\chi^{o\prime}/\chi^o(\xi=\xi_0)=\xi_0/(\xi_0^2-1)$.

For each value of R, we consider the following symmetries $\tilde{l}\lambda$: $\tilde{s}\sigma$, $\tilde{p}\sigma$, $\tilde{d}\sigma$, $\tilde{f}\sigma$, $\tilde{p}\pi$, $\tilde{d}\pi$, $\tilde{f}\pi$, $\tilde{d}\delta$, and $\tilde{f}\delta$, and for each of these we include the ten lowest radial states in the closed one-electron basis, thus obtaining a total of 90 closed-type one-electron functions. For $R=5$ we have found it necessary to include also $\tilde{l}=4$ functions. For both the $^1\Sigma_u^+$ and the $^1\Pi_u$ symmetry we use a closed-type two-electron basis including about 200 configurations constructed from the monoelectronic functions. A selection criterion involving a cutoff energy is used to extract these from the much larger set of two-electron functions y_{ij}^c that can be constructed with the one-electron closed-type basis. The open two-electron basis functions y_{ij}^o are selected to be those with energies closest to the total energy E. Le Rouzo and Raseev [9] have shown that the number of nontrivial solutions Ψ_β of the generalized eigenvalue system Eqs. (9) and (10) corresponds to the rank of the Λ matrix. In atomic problems this number equals the number of asymptotic channels taken into account explicitly. This is not strictly true in the molecular case because of the nonorthogonality of the elliptical harmonics [see Eq. (12)] [32]. However, when open two-electron basis functions y_{ij}^o are chosen whose energies are close to the total energy, the nonorthogonality is quite small. In practice we have always found the correct number of nontrivial solutions. Convergence of each variational R-matrix calculation was checked by recalculating each b_β from the eigenfunctions Ψ_β according to [8]

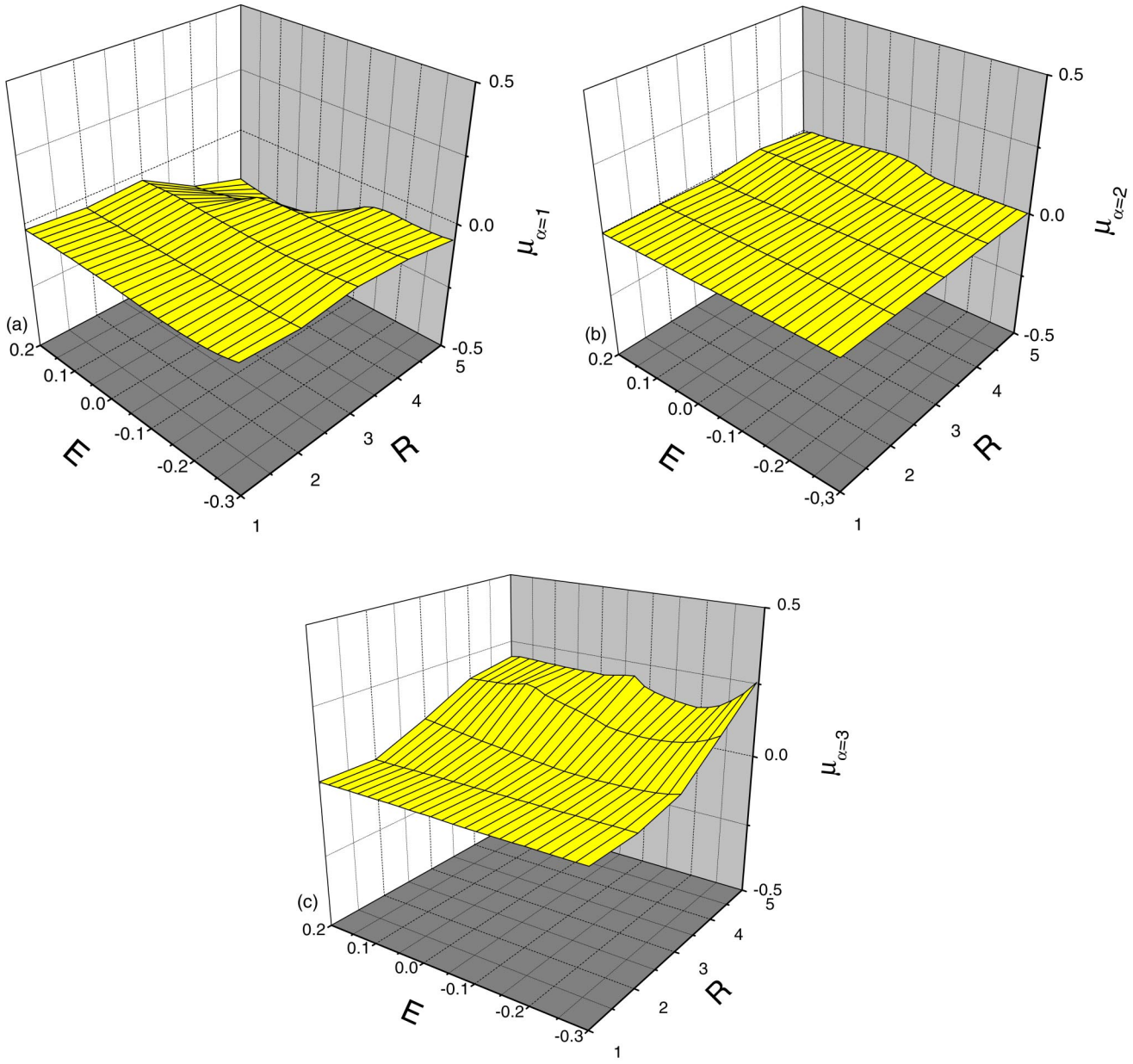

FIG. 2. *Ab initio* eigenquantum defects for $^1\Pi_u$ symmetry. (a) $\alpha=1$, (b) $\alpha=2$, (c) $\alpha=3$. (Cf. caption for Fig. 1.)

$$b_\beta \approx \frac{\int_\Sigma \Psi_\beta(\omega)\Psi'_\beta(\omega)d\omega}{\int_\Sigma \Psi_\beta(\omega)\Psi_\beta(\omega)d\omega}, \tag{23}$$

and ensuring that the b value thus obtained was close to the corresponding value obtained in the solution of the generalized eigenvalue system Eq. (9). The calculations have been carried out on a coarse grid of internuclear distances (1 bohr) and on an intermediate grid of energies (about 0.02 Ry).

IV. RESULTS AND DISCUSSION

A. *E* and *R* dependence of quantum defects

A convenient and compact way of visualizing the results is to plot the eigenquantum defects μ_α defined as

$$\mu_\alpha(E,R) = \frac{1}{\pi}\tan^{-1}\sum_{kk'} U^{-1}_{\alpha k} K_{kk'} U_{k'\alpha} \tag{24}$$

as functions of R and E, where U is the eigenvector matrix of K. This is done in Figs. 1 and 2 which represent the $^1\Sigma_u{}^+$ and $^1\Pi_u$ symmetries, respectively.

Inspection of the eigenvector matrix $U(E,R)$ (not shown) indicates that the $^1\Sigma_u^+$ eigensolutions 2 and 4 in Fig. 1 correspond quite closely to the $1\tilde{s}\sigma\epsilon\tilde{f}\sigma$ and $2\tilde{p}\sigma\epsilon\tilde{d}\sigma$ channels: we see that these eigenquantum defects are nearly zero in the low-energy range for all R values as one would expect on physical grounds because of the nearly nonpenetrating nature of the $\tilde{d}$ and $\tilde{f}$ electrons. These quantum defects begin to deviate significantly from zero only for higher energies (essentially above the $1\tilde{s}\sigma$ threshold) and larger R values,

again in line with physical expectations. By contrast, the eigenquantum defects $\alpha=1$ and 3 are more ''active''. As a consequence of strong configuration interaction they correspond to approximate 1:1 antisymmetric and symmetric mixtures of the $1\tilde{s}\sigma\epsilon\tilde{p}\sigma$ and $2\tilde{p}\sigma\epsilon\tilde{s}\sigma$ channels throughout the R range shown. We see in particular that at the low-energy edge the $\alpha=1$ eigenquantum defect increases quite significantly between $R=2$ and $R=3$, although this increase is attenuated for higher energies. This behavior is the consequence of the fact that for low energy and for increasing R the $^1\Sigma_u^+$ symmetry converts to the ionic channel ($H^+ + H^-$) [33]. The $^1\Pi_u$ eigenquantum defects shown in Fig. 2 are basically similar but on the whole less dependent on R and E. The eigensolutions $\alpha=1,2,3$ correspond approximately to $1\tilde{s}\sigma\epsilon\tilde{p}\pi$, $1\tilde{s}\sigma\epsilon\tilde{f}\pi$, and $2\tilde{p}\sigma\epsilon\tilde{d}\pi$ except for larger R where increasing configuration mixing causes $\alpha=2$ and 3 to become mixtures of $1\tilde{s}\sigma\epsilon\tilde{f}\pi$ and $2\tilde{p}\sigma\epsilon\tilde{d}\pi$. The data displayed in Figs. 1 and 2 demonstrate that the quantum defects will be amenable to the interpolation procedures required when one desires to take account of the nuclear degrees of freedom.

B. Potential-energy curves and "halfium" model

The accuracy and the predictive power of the quantum-defect surfaces of Figs. 1 and 2 can be tested in various ways. First we use them to calculate several of the lowest bound levels and to compare the resulting energies $U_n(R)$ with the corresponding accurate *ab initio* potential-energy curves for the B, B', and B'' and three higher $^1\Sigma_u^+$ states, and the C and D and two higher $^1\Pi_u$ states.

Generalized quantum-defect theory yields the positions of bound states as the solutions of the MQDT secular equation [1,2]

$$\det\left|\tan\beta_k(\epsilon_c)\,\delta_{kk'}+K_{kk'}(E)\right|=0 \tag{25}$$

for each R value individually, where the accumulated phase β_c is evaluated using the recipes given in Ref. [24] (cf. Sec. II E). Equation (25) yields the full spectrum of eigenvalues $U_n(R)$ from $n=2$ to high values. These eigenvalues are equivalent to the molecular potential energies once the proton-proton interaction term $+2/R$ (in rydbergs) has been added.

Before discussing the actual results, we shall comment on the accumulated phase parameters $\beta_k(\epsilon_c)$ [Eq. (15)] which appear in Eq. (25). Figure 3 displays these quantities calculated for $R=2$ and $^1\Sigma_u^+$ overall symmetry. The data refer to the radial channel functions $\epsilon\tilde{p}\sigma$, $\epsilon\tilde{f}\sigma$ and $\epsilon\tilde{s}\sigma$, $\epsilon\tilde{d}\sigma$, respectively, and are displayed for each channel as functions of the Coulombic effective principal quantum number $\nu_c=(-\epsilon_c)^{-1/2}$ (thick lines in the figure). In the absence of a core, bound levels would occur in each channel at the energies for which $\beta_k(\epsilon_c)$ is equal to an integer. The straight diagonal (thin) lines in Fig. 3 correspond to the phase parameters for a pure Coulomb field, $\beta_k^{coul}(\epsilon_c)=\pi(\nu_c-l)$, and are shown for comparison. They illustrate the well-known fact that the Rydberg equation (β_k^{coul}) yields

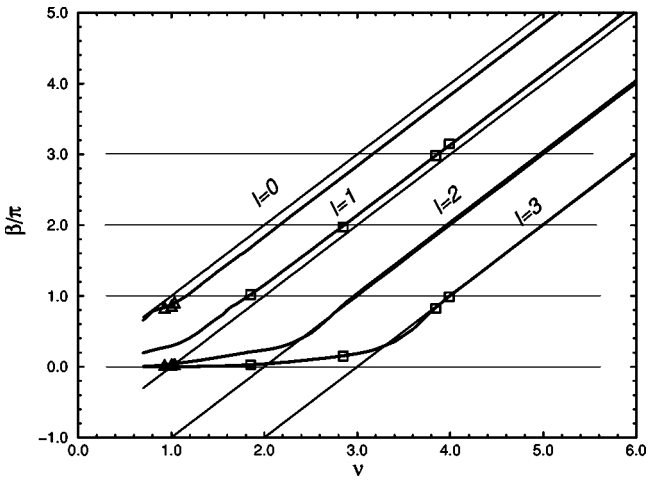

FIG. 3. Accumulated phase parameters β in units of π plotted as functions of the effective principal quantum numbers $\nu=(-\epsilon)^{-1/2}$ for $l=0-3$ and $\lambda=0$. Thick lines, numerical values calculated in Sec. II E. The thin lines correspond to the phase parameter $\beta/\pi=\nu-l$ for a Coulomb field, used in ordinary quantum-defect theory. The squares and triangles indicate the positions with respect to each channel of the four lowest states obtained by solving the full Eq. (25) (cf. the text).

unphysical levels at low energies corresponding to a zero or negative accumulated phase. These unphysical levels are avoided in the Milne approach since the numerical $\beta_k(\epsilon_c)$ tend asymptotically to zero for low energies.

The difference between numerical (elliptical) and analytic (Coulombic) accumulated phase values is seen to be nearly constant for each $\tilde{l}$ value and all but the lowest ν values. This difference therefore amounts to an energy-independent contribution to the quantum defect which arises outside the reaction boundary ξ_0 and is due to the combined effects of the quadrupole (plus higher multipole) moments created by the two half-charges (cf. Sec. II E) on each center as well as the polarization field. Mulliken [34], several decades ago, pioneered similar ideas when he developed his ''Demi-H_2^+'' model for the Rydberg states of H_2. He showed that the quantum defects near equilibrium could be interpreted as corresponding to the sum of a ''core-splitting'' contribution (included in the present work in the elliptical accumulated phases) and a ''penetration'' contribution (included here in the K matrix). The half-charged ion H_2^+ with an associated electron thus emerges as a hypothetical neutral ''particle''—which one might be tempted to call ''halfium''—which in Rydberg states of symmetrical diatomic molecules plays the role of the hydrogen atom in atomic physics. Obviously, as Mulliken [33] already pointed out, this type of one-electron model may be expected to be realistic in even-electron molecules only up to two or three times the equilibrium internuclear distance.

Tables I and II list the lowest few bound states of $^1\Sigma_u^+$ and $^1\Pi_u$ symmetries, obtained by solution of the full equation (25) including the K matrix, and compare them with the best currently available quantum-chemical *ab initio* calculations (Staszewska and Wolniewicz [35,36]). Tables I and II give the calculated effective principal quantum numbers $\nu(R)$ evaluated by using

TABLE I. Clamped-nuclei effective Rydberg principal quantum numbers for $^1\Sigma_u^+$ states of H_2. R is the internuclear distance in a.u. ν is the effective principal quantum number, Eq. (26). *Ab initio values* evaluated from the energies given by Staszewska and Wolniewicz [35,36]. The indicated orbital designations are valid for small R values only.

		$R=1$			$R=2$			$R=3$			$R=4$			$R=5$		
	State	$\nu_{ab\ initio}$	$\nu_{present}$	$\Delta\nu$	$\nu_{ab\ initio}$	$\nu_{present}$	$\Delta\nu$	$\nu_{ab\ initio}$	$\nu_{present}$	$\Delta\nu$	$\nu_{ab\ initio}$	$\nu_{present}$	$\Delta\nu$	$\nu_{ab\ initio}$	$\nu_{present}$	$\Delta\nu$
1	$2p\sigma B$	1.965	1.971	−0.006	1.829	1.854	−0.025	1.690	1.720	−0.030	1.625	1.647	−0.022	1.620	1.648	−0.028
2	$3p\sigma B'$	2.966	2.969	−0.003	2.821	2.847	−0.026	2.636	2.681	−0.045	2.422	2.474	−0.052	2.212	2.219	−0.007
3	$4p\sigma B''$	3.966	3.973	−0.007	3.817	3.844	−0.027	3.620	3.660	−0.040	3.368	3.366	+0.002	3.171	3.166	+0.005
4	$4f\sigma$	3.996	3.997	−0.001	3.986	3.990	−0.004	3.965	3.956	+0.009	3.914	3.942	−0.028	3.640	3.726	−0.086
5	$5p\sigma$	4.966	4.972	−0.006	4.815	4.842	−0.027	4.612	4.648	−0.036	4.333	4.299	+0.034	4.070	4.088	−0.018
6	$5f\sigma$	4.996	4.997	−0.001	4.986	4.990	−0.004	4.964	4.975	−0.011	4.903	4.937	−0.034	4.434	4.447	−0.014
7	$6p\sigma$		5.972			5.840			5.641			5.255			4.943	
8	$6f\sigma$		5.997			5.989			5.974			5.933			5.300	

$$U_n(R)=U^+(R)-\frac{1}{\nu^2(R)}. \tag{26}$$

Equation (26) assumes that the electronic energies here are in rydbergs and that $U^+(R)$ is the lowest H_2^+ $(1\tilde{s}\sigma)$ clamped-nuclei potential energy. Where a quantum-chemical *ab initio* potential curve is available, the difference $\Delta\nu$ (*ab initio* present) is given in the third column for each R value. Remember that an error of $\Delta\nu=0.05$ corresponds to an energy shift of about 1300 cm^{-1} for $\nu=2$, of 90 cm^{-1} for $\nu=5$, and of 10 cm^{-1} for $\nu=10$. The calculations of Refs. [35] and [36] on the other hand are accurate to within one or a few wave-number units (10^{-5} Ry), and therefore may be considered as being exact for the present purposes. The errors displayed in Tables I and II range up to about 0.05 for the $^1\Sigma_u^+$ and $^1\Pi_u$ states. Exceptions are the $^1\Sigma_u^+$ and $^1\Pi_u$ states with $\nu\approx3.7$ for $R=5$ where the deviation is somewhat larger. We have found that an increase of the variational basis always leads to an improved agreement as should, of course, be expected.

In Table III we compare the differences $\Delta=\nu_{ab\ initio}-\nu_{R\text{-}matrix}$ of this work (Table I) with those obtained by Greene and Yoo [7,29] for $^1\Sigma_u^+$ symmetry. It can be seen that in spite of the very different quantum defects resulting in the two sets of calculations (compare our Fig. 1 with Fig. 18 of Ref. [29]), the predictions for bound states are by and large of the same quality. While the earlier calculations appear to account a little better for the p manifold of states than our computations, our f states come closer to the *ab initio* values than theirs, no doubt because of our inclusion of polarization in the asymptotic region. For example, the $4f\sigma$ state has a quantum-defect of $\mu=n-\nu=0.035$ for $R=3$, both according the quantum-chemical calculations and experiment (see Fig. 4 below). This value compares more favorably with the present value 0.044 than with the value 0.009 derived from Ref. [29] (Table III).

Returning once again to the accumulated phase values, we consider once more Fig. 3 where the positions of the four lowest states from Table I for $R=2$ are indicated by squares and triangles with respect to each channel. The $2\tilde{p}\sigma\epsilon\tilde{d}\sigma$ channel (for all four states) and the $1\tilde{s}\sigma\epsilon\tilde{f}\sigma$ channel (for the two lowest states) are seen to be strongly closed at the corresponding energies with $\beta_k(\epsilon_c)$ close to zero, while $1\tilde{s}\sigma\epsilon\tilde{p}\sigma$ is weakly closed with $\beta_k(\epsilon_c)\approx1$ or larger. The core-excited $2\tilde{p}\sigma\epsilon\tilde{s}\sigma$ channel corresponds to an intermediate situation since $\beta_k(\epsilon_c)<1$ but not $\ll1$. It turns out that this latter channel indeed contributes strongly to the B, B', and B'' states.

C. Effective single-core quantum defects

Another test of the quantum defects is provided by comparison with the quantum-defect curves used previously in rovibronic multichannel quantum defect calculations for H_2. Among the most recent curves of this type are those published by Jungen and Ross [37], who determined energy and R dependent quantum-defect curves $\mu(E,R)$ defined by Eq. (26) with $\mu=n-\nu$ (ν integer) for the $1\tilde{s}\sigma\epsilon\tilde{p}\sigma$ and $1\tilde{s}\sigma\epsilon\tilde{p}\pi$

TABLE II. Clamped-nuclei effective Rydberg principal quantum numbers for $^1\Pi_u$ states of H_2. See caption for Table I.

		$R=1$			$R=2$			$R=3$			$R=4$			$R=5$		
	State	$\nu_{ab\ initio}$	$\nu_{present}$	$\Delta\nu$	$\nu_{ab\ initio}$	$\nu_{present}$	$\Delta\nu$	$\nu_{ab\ initio}$	$\nu_{present}$	$\Delta\nu$	$\nu_{ab\ initio}$	$\nu_{present}$	$\Delta\nu$	$\nu_{ab\ initio}$	$\nu_{present}$	$\Delta\nu$
1	$2p\pi C$	2.035	2.037	−0.002	2.080	2.075	+0.005	2.116	2.112	+0.004	2.126	2.127	−0.001	2.107	2.104	+0.003
2	$3p\pi D$	3.037	3.042	−0.005	3.080	3.087	−0.007	3.115	3.123	−0.008	3.125	3.118	+0.007	3.106	3.049	+0.057
3	$4f\pi V$	3.997	3.996	+0.001	3.989	3.992	−0.003	3.972	3.977	−0.005	3.931	3.945	−0.014	3.790	3.853	−0.063
4	$4p\pi D'$	4.037	4.039	−0.002	4.080	4.090	−0.010	4.113	4.121	−0.008	4.123	4.109	+0.014	4.105	4.053	+0.052
5	$5f\pi$		4.995			4.992			4.975			4.939			4.792	
6	$5p\pi$		5.037			5.090			5.119			5.105			5.058	

TABLE III. Comparison of *R*-matrix calculated effective principal quantum numbers for $^1\Sigma_u^+$ states of H_2. *Ab initio* values from Table I.

	$R=1$			$R=2$			$R=3$			$R=4$			$R=5$		
	$\nu_{ab\ initio}$	$\Delta\nu^a$	Ref. [29]^b	$\nu_{ab\ initio}$	$\Delta\nu^a$	Ref. [29]^b	$\nu_{ab\ initio}$	$\Delta\nu^a$	Ref. [29]^b	$\nu_{ab\ initio}$	$\Delta\nu^a$	Ref. [29]^b	$\nu_{ab\ initio}$	$\Delta\nu^a$	Ref. [29]^b
1 $2p\sigma$	1.965	−0.006	−0.004	1.829	−0.025	−0.011	1.690	−0.030	−0.013	1.625	−0.022	−0.013	1.620	−0.028	−0.014
2 $3p\sigma$	2.966	−0.003	−0.008	2.821	−0.026	−0.020	2.636	−0.045	−0.030	2.422	−0.052	−0.022	2.212	−0.007	−0.022
3 $4p\sigma$	3.966	−0.007	−0.008	3.817	−0.027	−0.018	3.620	−0.040	−0.022	3.368	0.002	−0.012	3.171	0.005	0.003
4 $4f\sigma$	3.996	−0.001	−0.003	3.986	−0.004	−0.011	3.965	0.009	−0.026	3.914	−0.028	−0.059	3.640	−0.086	−0.182
5 $5p\sigma$	4.966	−0.006	−0.008	4.815	−0.027	−0.017	4.612	−0.036	−0.020	4.333	0.034	0.000	4.070	−0.018	0.018
6 $5f\sigma$	4.996	−0.001	−0.004	4.986	−0.004	−0.010	4.964	−0.011	−0.023	4.903	−0.034	−0.054	4.434	−0.014	−0.044

[a]Present work.

[b]Yoo. $\Delta\nu=\nu_{ab\ initio}-\nu_{R-matrix}$ values.

channels. When combined with the rovibrational frame-transformation quantum-defect approach, these quantum defects reproduce the high Rydberg levels with ν up to ≈ 30 [38] observed in the absorption spectrum of H_2 with an accuracy of about 1 cm^{-1}, and they have been used successfully in a number of applications, including, e.g., wave-packet motion in preionized and predissociated states of H_2 [39]. These quantum-defect curves are based, on the one hand, on the five lowest *ab initio* potential-energy curves, and on the other hand, on the experimental observations for $\nu\approx 7$. Figure 4 displays the values obtained in Ref. [37] for near-threshold energies (full and dashed lines). Similarly, Uy *et al.* [40] presented analogous quantum-defect curves for the $1\tilde{s}\sigma\epsilon\tilde{f}\lambda$ ($\lambda=0-3$) channels of H_2 which were evaluated theoretically in the framework of a long-range force model for the electron-core interaction and which reproduce the observed nf levels of H_2 to within a fraction of 1 cm^{-1}. These curves are also shown in Fig. 4 for $\lambda=0$ and 1 by full and dashed lines, respectively. The + and × symbols in Fig. 4(a) correspond to the $^1\Sigma_u^+$ and $^1\Pi_u$ values obtained in the present approach with Eq. (26) for $\nu\approx 7$ (not included in Tables I and II). Figure 4(b) contains the corresponding data obtained for $\nu\approx 4$ from Tables I and II.

We see that the agreement is excellent in Fig. 4(a) near equilibrium ($R=2$), whereas large deviations occur for $R=4$ and $R=5$ for both the $^1\Sigma_u^+$ and $^1\Pi_u$ channels. Figure 4(b) on the other hand displays much better overall agreement, although near equilibrium our values deviate somewhat more from the empirical curves than in Fig. 4(a). The reason for these deviations is the following: the quantum-defect determinations in Ref. [37] used the near-threshold absorption spectrum near the $v^+=0$, 1, and 2 vibrational thresholds of the H_2^+ ground state. Levels in this range corresponding to high vibrational quantum numbers (where the nuclei explore separations beyond $R\approx 3$) correspond to relatively low electronic excitation, $\nu\approx 4$, whereas levels corresponding to low vibrational quantum number (where nuclear motion remains restricted to the equilibrium region) correspond to higher electronic excitation. We conclude that the empirical quantum-defect curves of Ref. [37] are thus probably more *effective* than had previously been thought, because in fact they represent a compromise since they corre-

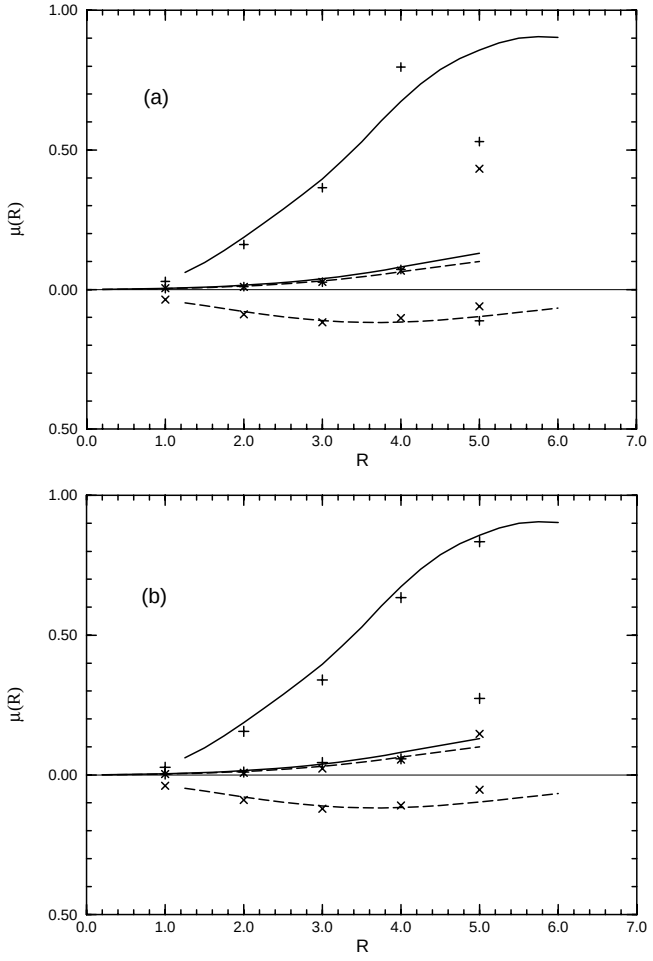

FIG. 4. Effective one-channel quantum defects for $p\lambda$ and $f\lambda(\lambda=0,1)$ Rydberg series converging to the H_2^+ ground state. Full lines represent $p\sigma$ and $f\sigma$ quantum defects from Refs. [37] and [40], respectively. Dashed lines: corresponding $p\pi$ and $f\pi$ quantum defects. Symbols + (×) correspond, respectively, to the present potential curve calculations from Table I (Table II) for $^1\Sigma_u^+$ ($^1\Pi_u$) symmetry. (a) for $\nu\approx 7$, (b) for $\nu\approx 4$.

TABLE IV. Positions and widths of the lowest doubly excited $^1\Sigma_u^+$ resonances in H_2.

R[a]	E[b]	$2\tilde{p}\sigma 2\tilde{s}\sigma$ $\nu_{present}$[c]	Ref. [47]	Ref. [7]	E	$\nu_{present}$	$2\tilde{p}\sigma 3\tilde{s}\sigma$ Ref. [47]	Ref. [29]	E	$2\tilde{p}\sigma 3\tilde{d}\sigma$ $\nu_{present}$	Ref. [47]	Ref. [7]
1.0	1.4810	1.847	1.821	1.819	1.6482	2.820	2.807	2.798	1.6660	3.043		
2.0	0.6226	2.010	2.016	1.996	0.7611	3.028	3.032	3.021	0.7585	2.991		
3.0	0.1946	2.111	2.249	2.246	0.3167	3.128			0.3043	2.954	3.021	2.987
4.0	0.0624	2.685	2.634	2.371	0.1288	3.719			0.0829	2.909	3.070	2.907
R		$\Gamma_{present}$[d]	Ref. [47]	Ref. [7]		$\Gamma_{present}$	Ref. [47]	Ref. [29]		$\Gamma_{present}$	Ref. [47]	Ref. [29]
1.0		0.020	0.018	0.022		0.005	0.004	0.005		0.0004		
2.0		0.048	0.049	0.054		0.002[e]	0.002	0.004		0.002[e]		
3.0		0.059	0.065	0.090		0.028[e]				0.009[e]	0.004	0.004
4.0			0.040			0.013[e]				0.030	0.024	0.021

[a]Internuclear distance in bohr.

[b]Present work. Energy above $1\tilde{s}\sigma$ in rydbergs, evaluated by eliminating the open channels from Eq. (25).

[c]Effective principal quantum number with respect to the $2\tilde{p}\sigma$ ion threshold.

[d]Width (rydbergs).

[e]Overlapping resonance.

spond to high ν values near $R\approx 2$ but to much lower ν values for $R=4$ and 5. The first-principles calculations further indicate that near $R=4$ and 5 the doubly excited states $2\tilde{p}\sigma 2\tilde{s}\sigma$ and $2\tilde{p}\sigma 3\tilde{d}\pi$ cross the ion ground-state curve and cause a series of avoided crossings in the bound-state manifold (cf. Tables IV and V of the present paper and Fig. 2 of Ref. [7] where the $^1\Sigma_u^+$ perturbations are illustrated). It is these avoided crossings that cause the disrupted behavior of the theoretical defects in Fig. 4(a) for $R\geqslant 4$.

D. Doubly excited resonances

A final test of the quantum-defect matrices calculated in the present work consists in comparing the resonance positions and widths corresponding to the $2\tilde{p}\sigma n\tilde{l}\lambda$ lowest doubly excited $^1\Sigma_u^+$ and $^1\Pi_u$ configurations with previous *ab initio* work. The calculation is made again by solving Eq. (25) with the K matrices calculated in this work. The only difference is that now the two channels $1\tilde{s}\sigma\epsilon\tilde{p}\lambda$ and $1\tilde{s}\sigma\epsilon\tilde{f}\lambda$ for $\lambda=0$ or 1 are open, so that the corresponding accumulated phases $\beta_k(\epsilon_c)$ must be replaced by the negative of the eigenphase $\pi\tau_\rho(E)$ which we are looking for. Equation (25) then in effect becomes a generalized eigenvalue problem as detailed in the QDT literature [2]. The eigenphase sum $\tau_{\rho=1}+\tau_{\rho=2}$ obtained in this way increases by one unit near the $2\tilde{p}\sigma n\tilde{l}\lambda$ resonances. The resonance position corresponds to the energy where the energy derivative of the eigenphase sum has a maximum, while the width corresponds to the half-width of this rise. The resonance positions can alternatively be calculated as bound-state positions by eliminating the open channels from Eq. (25). We have found that as long as the resonances are narrow and well isolated the two ways of calculating the positions give identical results, showing that the resonance shifts are small in these cases. However, when the resonances are broad and begin to overlap, we observe differences. At the same time the concept of the position and width of an individual resonance

TABLE V. Positions and widths of the lowest $^1\Pi_u$ doubly excited resonances in H_2, See caption for Table IV.

R	E	$2\tilde{p}\sigma 3\tilde{d}\pi$ $\nu_{present}$	Ref. [47]	E	$2\tilde{p}\sigma 4\tilde{d}\pi$ $\nu_{present}$	Ref. [47]
1.0	1.6609	2.974	3.198	1.7103	3.963	4.095
2.0	0.7589	2.998	3.048	0.8078	4.002	3.940
3.0	0.3056	2.969	3.014	0.3560	3.974	3.999
4.0	0.0878	2.957	3.070	0.1383	3.979	4.030
R		$\Gamma_{present}$	Ref. [47]		$\Gamma_{present}$	Ref. [47]
1.0		0.0002	0.0024		0.0001	0.0002
2.0		0.0012	0.0009		0.0008	0.0060
3.0		0.0048	0.0033		0.0027	0.0019
4.0		0.0102	0.0126		0.0053	0.0058

loses its meaning and one can at best give estimates of these quantities.

Tables IV and V give the effective principal quantum numbers ν of the resonance positions calculated with respect to the $2\tilde{p}\sigma$ first-excited potential-energy curve of H_2^+, and also their widths. The lowest resonance has been calculated by many authors [16,41–46]. For comparison we include in the Tables IV and V the positions and widths given by Tennyson [47] and Greene and Yoo [7,29]. We have found that the $2\tilde{p}\sigma n\tilde{s}\sigma$ and $2\tilde{p}\sigma n\tilde{d}\sigma$ resonances for $n\geqslant 3$ are strongly overlapping and in fact cross over with increasing R. Thus according to our calculations (Table IV) the $3\tilde{d}\sigma$ resonance lies above $3\tilde{s}\sigma$ up to $R=2$ but below it for $R\geqslant 2$, and we find that strong $\tilde{l}$ mixing occurs in the (anti) crossing region. An analogous $s\sigma\approx d\sigma$ anticrossing is known to occur in the ${}^3\Sigma_g^+$ manifold of states associated with the ground-state H_2^+ core [48]. This phenomenon has apparently been overlooked in Refs. [47] and [29] where only the lower partner of the pair was calculated. Tables IV and V show that apart from this aspect there is good agreement between the present and the previous calculations.

V. CONCLUSION

We believe that the present work constitutes a decisive step towards the goal of calculating fully R-matrix *ab initio* photoionization and photodissociation spectra of highly excited H_2 at the rotational-vibrational level. What is needed to achieve this goal is: (i) sufficiently accurate quantum defect matrices and (ii) a smooth behavior of these matrices as functions of R and E. The smoothness in R is necessary so that the quantum defects can be interpolated on a fine R mesh as required for successful inclusion of the vibrational degree of freedom. The smoothness both in R and E is necessary in order to be able to use the frame-transformation scheme, which is known to fail when the quantum defects or K matrices depend strongly on energy [5].

Before we can actually calculate *ab initio* photoionization and photodissociation spectra, two steps must be implemented. First, we must transform the present elliptical quantum-defect matrices into a spherical representation by matching the variational solutions Ψ_β of Eq. (16) to spherical asymptotic channel functions expressed in terms of spherical harmonics $Y_{lm}(\theta,\varphi)$. This work is underway and is required so that the vector coupling techniques for coupling l to the core rotational momentum can be carried out. A second aspect to be considered in the near future concerns the calculation of the molecule-fixed components of the dipole transition operator as functions of R and E, necessary for the evaluation of photoabsorption cross sections.

A noteworthy feature of the present results is that the quantum-defect matrix elements $\mu_{kk'}$ can be interpolated directly on a fine R mesh after the R-matrix treatment has been carried out. In this way the choice of the basis functions in the internal zone can be adjusted flexibly for each R individually. This was not the case in the previous work [7] where the interpolation had to be carried out at the level of the Γ and Λ matrices of Eqs. (11) and (12), which means that the same configurations had to be used for all R values calculated. Note further that we will not need to calculate quantum-defect matrices for R values larger than about 6 a.u., because outside this range we will treat R as the dissociation reaction coordinate in an approach that has been outlined, e.g., in Ref. [49].

Another aspect of the present work is that our use of elliptical coordinates combined with inclusion of polarization in the external zone allows us to reduce the R-matrix radius significantly. Therefore it has been possible to describe valence-type states in a Rydberg-channel representation, whereas, for example, in the work of Ref. [20] on NO the R-matrix radius was taken roughly three times larger, and the valence-type states are contained entirely inside the reaction volume and manifest themselves as R-matrix poles.

We finally wish to comment on the physical meaning of the quantum-defect matrices such as illustrated by Figs. 1 and 2. They have been optimized by a careful choice of the regular and irregular basis functions in each of the ''strongly closed'' channels, based on the considerations of Ref. [24]. It should be realized that depending on the optimization, different sets of basically equivalent short-range quantum-defect matrices can be obtained. Thus, for example, the matrices given by Greene and Yoo [7,29] exhibit much stronger variations in R and E (and are therefore probably less ''physically meaningful''), but are equally successful as ours in reproducing the lowest fixed-nuclei potential energies $U_n(R)$ which are quantum-mechanically strictly defined quantities. The fact that an infinite number of physically equivalent quantum-defect matrices can be obtained is easily understood from Eq. (21), which expresses the matching of the internal and external solutions of the Schrödinger equation. For each closed channel we may make the substitution $\overline{f}=Cf$, $\overline{g}=C^{-1}g-Df$, where C and D are arbitrary constants which may be energy dependent. The base pair $(\overline{f},\overline{g})$ is formally equivalent to the pair f,g since the regular/irregular behavior near $\xi=1$ is preserved and the Wronskian is also unchanged. However the resulting K and μ matrices will obviously be different. One therefore has to abandon the concept of a ''unique'' quantum defect. At the same time however, vast possibilities of optimization open up such as we have begun to implement in this work, and it turns out that when well chosen, molecular quantum defects will still convey a comprehensive picture of the physics of Rydberg states.

ACKNOWLEDGMENTS

We thank S. Bezzaouia (Tunis) for extensive help during the development the computer codes. J.-M. Lecomte (Orsay) is thanked for helpful discussions concerning the formal aspects of R-matrix theory. The project was supported in part in the framework of a DGRST/CNRS Tunisian-French cooperation. Further support came from a grant of the French INSU (Physico-chimie du Milieu Interstellaire). M.T. acknowledges the hospitality of the Laboratoire Aimé Cotton during several visits.

APPENDIX

The associated Legendre functions of the first kind and the second kind are calculated by use of expansions over confluent hypergeometric functions (Ref. [50]). Note that a factor $\pi^{-1/2}$ appears to be missing in the second part of relation 8.1.5 of Ref. [50].

$$P_l^m(\xi)=\frac{(2l)!}{2^l(l-m)!l!}\frac{\xi^{l+m}}{(\xi^2-1)^{m/2}} \times F\left(-\frac{l+m}{2};\frac{1-l-m}{2};\frac{1-2l}{2};\frac{1}{\xi^2}\right), \quad \text{(A1)}$$

$$Q_l^m(\xi)=(-1)^m 2^l\frac{l!(l+m)!}{(2l+1)!}\frac{(\xi^2-1)^{m/2}}{\xi^{l+m+1}} \times F\left(\frac{2+l+m}{2};\frac{1+l+m}{2};\frac{3+2l}{2};\frac{1}{\xi^2}\right). \quad \text{(A2)}$$

These functions have the appropriate asymptotic behavior ($\xi\to\infty$) given by [26]

$$P_l^m(\xi)\sim\frac{(2l)!}{2^l(l-m)!l!}\xi^l, \quad \text{(A3)}$$

$$Q_l^m(\xi)\sim\frac{2^l l!(l+m)!}{(2l+1)!}\frac{1}{\xi^{l+1}}. \quad \text{(A4)}$$

The confluent hypergeometric functions $F(a,b,c,1/\xi^2)$ (Landau and Lifschitz [51]) are evaluated numerically by use of the series expansion:

$$F\left(a,b,c,\frac{1}{\xi^2}\right)=\sum_{n=0}^{\infty}U_n, \quad \text{(A5)}$$

where the series terms U_n are given by the recurrence relation

$$U_{n+1}=\gamma_n\left(a,b,c,\frac{1}{\xi^2}\right)U_n \quad \text{(A6)}$$

with $U_0=1$, and

$$\gamma_n\left(a,b,c,\frac{1}{\xi^2}\right)=\frac{1}{n+1}\frac{(a+n)(b+n)}{c+n}\frac{1}{\xi^2}. \quad \text{(A7)}$$

[1] M.J. Seaton, Rep. Prog. Phys. **46**, 167 (1983).
[2] C.H. Greene and Ch. Jungen, Adv. At. Mol. Phys. **21**, 51 (1985).
[3] J.M. Weber, E. Leber, M.-W. Ruf, and H. Hotop, Phys. Rev. Lett. **82**, 516 (1999).
[4] V. Kokoouline, C.H. Greene, and B.D. Esry, Nature (London) **412**, 891 (2001).
[5] C.H. Greene and Ch. Jungen, Phys. Rev. Lett. **55**, 1066 (1985).
[6] J.A. Stephens and V. McKoy, J. Chem. Phys. **97**, 8060 (1992).
[7] C.H. Greene and B. Yoo, J. Phys. Chem. **99**, 1711 (1995).
[8] C.H. Greene, Phys. Rev. A **28**, 2209 (1983).
[9] H. Le Rouzo and G. Raseev, Phys. Rev. A **29**, 1214 (1984).
[10] W. Kohn, Phys. Rev. **74**, 1763 (1948).
[11] S.C. Ross and Ch. Jungen, Phys. Rev. A **49**, 4353 (1994).
[12] G. Raseev and H. Le Rouzo, Phys. Rev. A **27**, 268 (1983).
[13] G. Raseev, J. Phys. B **18**, 423 (1985).
[14] J. Tennyson, C.J. Noble, and S. Salvini, J. Phys. B **17**, 905 (1984).
[15] J. Tennyson and C.J. Noble, J. Phys. B **18**, 155 (1985).
[16] I. Shimamura, C.J. Noble, and P.G. Burke, Phys. Rev. A **41**, 3545 (1990).
[17] J. Tennyson, J. Phys. B **21**, 805 (1988).
[18] B.K. Sarpal, S.E. Branchett, J. Tennyson, and L.A. Morgan, J. Phys. B **24**, 3685 (1991).
[19] I. Rabadan and J. Tennyson, J. Phys. B **29**, 3747 (1996); **30**, 1975 (1997).
[20] M. Hiyama and M.S. Child, J. Phys. B **35**, 1337 (2002).
[21] R.E. Stratmann, G. Bandarage, and R.R. Lucchese, Phys. Rev. A **51**, 3756 (1995).
[22] M. Arif, Ch. Jungen, and A.L. Roche, J. Chem. Phys. **106**, 4102 (1997).
[23] M. Aymar, C.H. Greene, and E. Luc-Kœnig, Rev. Mod. Phys. **68**, 1015 (1996).
[24] F. Texier and Ch. Jungen, J. Phys. B **33**, 2495 (2000).
[25] F.E. Harris, J. Chem. Phys. **32**, 3 (1960).
[26] F. Robicheaux, J. Phys. B **29**, 779 (1996).
[27] Q. Zheng, A.K. Edwards, R.M. Wood, and M.A. Mangan, Phys. Rev. A **52**, 3945 (1995).
[28] U. Fano and C.M. Lee, Phys. Rev. Lett. **31**, 1573 (1973).
[29] B. Yoo, Ph.D. thesis, Louisiana State University, Baton Rouge, Louisiana (unpublished).
[30] W.E. Milne, Phys. Rev. **35**, 863 (1933).
[31] D.M. Bishop and L.M. Cheung, J. Phys. B **11**, 3133 (1978).
[32] We thank J.-M. Lecomte for bringing this point to our attention.
[33] R.S. Mulliken, J. Am. Chem. Soc. **88**, 1849 (1966).
[34] R.S. Mulliken, J. Am. Chem. Soc. **91**, 4615 (1969).
[35] G. Staszewska and L. Wolniewicz, J. Mol. Spectrosc. **212**, 208 (2002).
[36] G. Staszewska and L. Wolniewicz, http://www.phys.uni.torun.pl/ftp/publications/ifiz/luwo/
[37] Ch. Jungen and S.C. Ross, *Molecular Hydrogen in Space*, edited by F. Combes and G. Pineau des Forêts (Cambridge University Press, Cambridge, 2000), p. 31.
[38] G. Herzberg and Ch. Jungen, J. Mol. Spectrosc. **41**, 425 (1972).
[39] F. Texier, Ch. Jungen, and S.C. Ross, Faraday Discuss. **115**, 71 (2000).

[40] D. Uy, C.M. Gabrys, T. Oka, B.J. Cotterel, R.J. Stickland, Ch. Jungen, and A. Wüest, J. Chem. Phys. **113**, 10143 (2000).
[41] H. Takagi and H. Nakamura, J. Phys. B **13**, 2619 (1980).
[42] H. Takagi and H. Nakamura, Phys. Rev. A **27**, 691 (1980).
[43] A.U. Hazi, J. Phys. B **8**, L262 (1975).
[44] T. O'Malley, J. Chem. Phys. **51**, 322 (1969).
[45] S. Guberman, J. Chem. Phys. **78**, 1404 (1983).
[46] L.A. Collins and B.I. Schneider, Phys. Rev. A **27**, 101 (1983).
[47] J. Tennyson, At. Data Nucl. Data Tables **64**, 253 (1996).
[48] C.B. Wakefield and E.R. Davidson, J. Chem. Phys. **43**, 834 (1965).
[49] A. Matzkin, Ch. Jungen, and S.C. Ross, Phys. Rev. A **62**, 062511 (2000).
[50] *Handbook of Mathematical Functions*, edited by M. Abramowitz and I. Stegun (Dover, New York, 1970).
[51] L. Landau and E. Lifschitz, *Quantum Mechanics* (Mir Editions, Moscow, 1966).